Insights on the UO2+x/U4O9 phase characterization in oxidized UO2 pellets as a function of the hyper-stoichiometry

C. Gaillard, H. Lotz, L. Sarrasin, Y. Pipon, R. Ducher, N. Moncoffre

Insights on the UO_{2+x}/U_4O_9 phase characterization in oxidized UO_2 pellets as a function of the hyper-stoichiometry

C. Gaillard[1]*, H. Lotz[1], L. Sarrasin[1], Y. Pipon[1,2], R. Ducher[3], N. Moncoffre[1]

[1] Univ Lyon, Univ Claude Bernard Lyon 1, CNRS/IN2P3, IP2I Lyon, UMR 5822, F-69622, Villeurbanne, France

[2] Univ Lyon, Univ Claude Bernard Lyon 1, IUT Lyon-1, Département chimie, F-69622, Lyon, France

[3] IRSN, LETR – BP3, 13115 St-Paul-Lez-Durance Cedex, France

*** Correspondence:**
Corresponding Author: gaillard@ipnl.in2p3.fr

Keywords: UO_2, oxidation, U_4O_9, Raman spectroscopy, HERFD-XANES

Abstract

We present new insights on the study of the UO_{2+x}/U_4O_9 equilibrium in UO_2 as a function of the hyper-stoichiometry x, by coupling HERFD-XANES at the uranium M_4-edge and micro-Raman spectroscopy mapping. XANES allowed to measure the uranium speciation in the samples while Raman spectroscopy was used to characterize individually the composition and localization of the different oxide phases. UO_2 pellets were oxidized under dry conditions at temperatures above the UO_{2+x}/U_4O_9 phase transition to reach hyper-stoichiometries in the range $0.01 \leq x \leq 0.1$. Combining both technics, we could determine the proportion between U_4O_9 and UO_{2+x}. We show that at low O/U ratio, U_4O_9 is present as small clusters inside UO_2 grains. As the O/U increases, we evidence the formation of a network of U_4O_9 crystallized inside UO_{2+x} grains. The variation of the UO_{2+x} phase hyper-stoichiometry (x) was evaluated as a function of the sample oxidation.

1. Introduction

Uranium oxide UO_2 is widely studied because of its use as nuclear fuel in nuclear Pressurized Water Reactor power plants. Among all the parameters that can affect the fuel performance, an important one is fuel oxidation. It can occur during normal reactor operations in the case of a defective rod or during reactor accident conditions. Under LOCA (Loss Of Coolant Accident) conditions, fuel oxidation will occur due to high temperatures and steam environment. It will affect the fuel thermal properties and the fission products release [1-3]. Understanding oxidation mechanisms and characterizing formed oxide phases are therefore important to apprehend all consequences resulting from this type of accident. Both kinetics of oxidation and crystallographic structures of the U-O oxide phases (α, β, γ- U_4O_9, U_3O_7, α and β- U_3O_8) have been studied extensively [4-10]. UO_2 has a fluorite structure Fm-3m. At high temperature, UO_2 oxidation forms a UO_{2+x} single phase where oxygen atoms are incorporated in the fluorite structure in interstitial octahedral sites. At lower temperature, UO_{2+x} coexists with α-U_4O_9 (= $UO_{2.25}$). In hyper-stoichiometric compounds, the charge balance is made by the valence change of uranium cations from U^{4+} to U^{5+} while interstitial oxygen atoms are accommodated as Willis clusters

involving two oxygen vacancies, two oxygen O' atoms and two O" atoms. A further increase of interstitial oxygen atoms leads to a distortion of the unit cell from cubic to tetragonal and ultimately to a monoclinic structure. The formation of U_4O_9 (and U_3O_7) involves a slight volume reduction while the formation of U_3O_8 involves a 36% volume increase.

The transition mechanism from UO_{2+x} to U_4O_9 has been widely investigated in term of phase transition, allowing to establish the U-O equilibrium phase diagram [11-18]. Only few authors studied the morphological changes in polycrystalline UO_2 after oxidative treatments. Whillock and Pearce studied the distribution and percentage of U_4O_9 in oxidized UO_2 (total O/U ratio between 2.05 and 2.12) [19]. The authors evidenced different types of morphology for U_4O_9 in UO_2, from needles to starbursts or massive blocks as the U_4O_9 proportion varies from 20 to 40%. Schaner studied the UO_2-U_4O_9 equilibrium phase diagram between $UO_{2.006}$ and $UO_{2.176}$ on polycrystalline UO_2 pellets using metallographic techniques [20]. Results evidenced that the U_4O_9 solubility in UO_{2+x} depends on temperature. In addition, photomicrographs of the sample surfaces taken after different oxidative treatments at 900°C show that the U_4O_9 morphology inside UO_{2+x} grains depends on the O/U ratio and on the experimental procedure used to cool the samples at ambient temperature (slow temperature decrease or quenching below the phase transition limit).

In this paper, we present a contribution to the study of the UO_{2+x}/U_4O_9 equilibrium in UO_2 as a function of the hyper-stoichiometry, by coupling HERFD-XANES at the uranium M_4-edge and micro-Raman spectroscopy mapping. XANES allowed to measure the uranium speciation in the samples while Raman spectroscopy was used to characterize individually the composition and localization of the different oxide phases in UO_2 pellets. Combining both technics, we could determine the proportion between U_4O_9 and UO_{2+x} and evaluate the variation of the UO_{2+x} phase stoichiometry (x) as a function the sample oxidation.

2. Materials and methods

2.1. Sample preparation

Depleted UO_2 pellets (diameter 9 mm x 1.6 mm thick) of high bulk density (97.5% of the theoretical density), sintered at 1750°C under reducing condition (Ar/H_2 5%) for 5 hours, were provided by Framatome. Their average grain size is 11 µm, which is comparable to that of the PWR nuclear fuel. Pellets were polished on one side by the PRIMEVerre company (Montpellier, France) with ¼ µm diamond paste. Then, samples were annealed in a PECKLY© tubular furnace at 1000°C for 10 hours under vacuum (10^{-7} mbar) to degas adsorbed species on the pellets. Secondly, an annealing at 1600°C for 4 hours in a NABERTHERM© tubular furnace was performed under a Ar/H_2 5% gas mixture flowing through ultrahigh capacity oxygen and moisture traps. This thermal treatment allows annealing of the polishing defects while avoiding UO_2 oxidation.

UO_2 oxidation was performed by thermal annealing under dry atmosphere using different protocols according to samples. A summary is presented in Table 1. Before and after each annealing, pellets were weighted with a Sartorius µ-balance with an accuracy of ±2 µg. The O/U ratio were calculated from the mass gain of the samples during annealing, with an error of ± 0.001.

Sample "*UO2_ox1_A*" and sample "*UO2_ox1_B*" correspond to the same initial pellet. For "*UO2_ox1_A"*, the pellet was annealed in a NABERTHERM© tubular furnace at 1600°C under an Ar/O_2 5 ppm gas flow during 4 hours, with a ramping of 300°/h for heating and cooling. After the annealing treatment, the pellet was weighted and analyzed by Raman spectroscopy. Then, the pellet was oxidized a second time following the same experimental protocol (sample *"UO2_ox1_B"*) to reach

a final O/U ratio of 2.010. Sample "*UO2_ox2"* was submitted to the same annealing treatment than sample "*UO2_ox1_B"* to reach a 2.010 stoichiometry. Then, it was annealed in a steel tubular furnace at 900°C during an hour under an Ar/O_2 5 ppm gas flow. According to the O/U phase diagram [14, 21], this annealing condition allows the dissolution of any U_4O_9 phase that might be present in the sample to form the sole UO_{2+x} phase. Then a sample quenching was performed with the aim to keep this UO_{2+x} phase at ambient temperature. This rapid sample cooling, from 900°C to room temperature, was achieved in ten minutes under the same atmospheric conditions as those during the annealing (Ar/O_2 5 ppm gas flow). After this quenching, no mass variation was detected on the pellet, so we can assume that its final stoichiometry is the same as before the quenching (2.010). Sample "*UO2_ox3*" was prepared by annealing at 1600°C under an Ar/O_2 5 ppm gas flow for 15 hours. Sample "*UO2_ox4*" was obtained using a SETARAM© thermobalance. The UO_2 pellet was placed in a quartz boat suspended on an oven. The analyzer was placed under vacuum for 30 min and then filled with a carrier gas to avoid any gaseous pollution. The gases used were He and Ar/O_2 100 ppm, the introduction of O_2 being controlled by an oxygen sensor. In order to reach O/U ratio = 2.10, the oxidation was carried out at a temperature of 850°C. A ramp of 10°C.min^{-1} was programmed up to 850°C, then a plateau at 850°C until the mass gain was reached, and finally the heating was switched off. O_2 was added only during the plateau at 850°C while the increase and decrease in temperature were performed under He. The mass gain was achieved in 3.5 hours. Figure S1 displays the mass gain variation with time and temperature; these curves show that the mass gain of the pellet is linear with time at 850°C. The change of atmosphere at the end of the plateau combined with the decrease of temperature (about 30°C/min) probably limits the oxidation to a negligible level during the cooling stage.

2.2. HERFD-XANES measurements at the U M_4-edge

High-energy resolution fluorescence detected XANES (HERFD-XANES) data were measured at the MARS beamline of the SOLEIL synchrotron (Saint-Aubin, France) [22] on pellets. Spectra were measured at room temperature at the U M_4-edge (3728 eV) using a double-crystal monochromator (DCM) equipped with a pair of Si(111) crystals. Higher harmonics rejection and vertical focusing were achieved using the Si strip of each mirror inserted before and after the DCM with a 4 mrad incidence angle. The beam size was 250x150 µm. The incident energy was calibrated using the absorption K-edge of potassium of a KBr pellet (3608.4 eV). HERFD-XANES was performed using the crystal-analyzer emission spectrometer in the Rowland geometry and a KETEK single-element silicon solid-state detector. The M_β emission line of U (3339 eV) was analyzed using the 220 reflection of a Si(220) bent, diced crystal analyzer with a curvature radius of 1 m. The samples were oriented at 45° with respect to the incident beam. A He-filled balloon was used to reduce the scattering of the incident and emitted X-rays by the air between the sample and the crystal analyzer and the detector. No evolution of the spectra was observed during measurements under the beam. Collected spectra were normalized using the ATHENA software [23]. The contribution of U(IV) and U(V) were derived from the linear combination of UO_2 and U_4O_9 reference spectra.

2.3. Raman analysis

Raman spectroscopy analyses were performed on a Renishaw Invia Qontor equipped with a grating 1800 gr/mm, using a He−Ne laser (633 nm). Mappings were recorded using a x50 objective from 200 to 1300 cm^{-1}. Great care has been taken to ensure that the laser does not induce any structural modification during the measurements. Starting with low to high laser powers, analyses were repeated on a same point on a pellet surface to optimize our measurement parameters and verify that Raman spectra do not change under the effect of beam. Thus, the incident laser power was fixed to 0.9 mW. A silicon standard was used to calibrate the spectrometer with its line frequency fixed at 520.5 cm^{-1}. Raman mappings were performed on UO_2 pellets with a spatial resolution of 1×1 µm^2. Each mapping

covers at least 10 grains and the depth probed is estimated to be between 3 and 5 µm [24]. Data processing was achieved using WIRE 5.4 software.

2.4. AFM

Atomic force microscopy (AFM) was performed on NaioAFM microscope (Liestal, Switzerland). NaioAFM was fitted with a 190 Al cantilever tip with the following dimensions: length, 225 µm; width, 38 µm; tip radius, 10 nm. The cantilever spring constant is 48 $N.m^{-1}$. Data analysis was performed using Nanosurf, Naio control software in dynamic mode. The AFM images were recorded in air and at room temperature. Data treatment was performed using Gwyddion software.

3. Results

3.1. Chemical state of uranium in oxidized samples

HERFD-XANES at the U M_4-edge probes the 5f unoccupied states and it has been shown to be suitable to differentiate U(V) species from U(IV) and U(VI) [25]. Therefore, we have used this technique on UO_2 oxidized samples in order to determine the uranium oxidation state. It must be noticed that at this edge, the UO_2 pellet is probed only over the first micrometer. Figure 1 displays the HERFD-XANES spectrum of a stoichiometric UO_2, compared with spectra of oxidized samples at different O/U ratio. The first peak at 3725.3 eV corresponds to U(IV) while the second peak observed at 3726.4 eV corresponds to the presence of U(V). This latter peak is thus the signature of a hyper-stoichiometry.

UO_2 oxidation can lead to the formation of different species: UO_{2+x} which is a mixture of U(IV) and U(V); U_4O_9 that is composed of 50% of U(IV) and 50% of U(V), and U_3O_8 containing a mixture of U(V) and U(VI) [26]. We did not consider the latter oxide as we do not evidence any U(VI) signal, which was further confirmed by Raman analysis (see below). Thus, spectra were fitted by linear combination of U(IV) and U(V) reference spectra in order to determine the proportion between uranium oxidation degrees. Table 2 gives these results and the O/U ratio calculated from this proportion. The less oxidized sample, "*UO2_ox1_B",* contains about 10% of U_4O_9. Sample "*UO2_ox3"* contains 30 % of U_4O_9 and a stoichiometry at the surface which is slightly higher than the average one obtained by mass gain measurements (O/U = 2.08 vs. 2.05). Analysis of the "*UO2_ox4*" sample shows a noticeable higher hyper-stoichiometry at the extreme surface (2.16) than the average one (2.10), and the presence of 65 % of U_4O_9.

3.2. Speciation of uranium oxide phases by Raman spectroscopy

Raman spectroscopy was used to identify the different crystallographic phases that may be present in samples after oxidation. Three phases are expected: stoichiometric UO_2, UO_{2+x} and U_4O_9. Their respective Raman spectra are shown in Supplementary Information (figure S2) and Raman mappings of stoichiometric UO_2 were published in [27]. For stoichiometric UO_2, the most intense band is the T_{2g} band located at 444.6 cm^{-1}, typical from the fluorite structure. This triply degenerate mode corresponds to the symmetrical vibration of oxygen atoms around an uranium atom [28]. The second most intense band located at ~1150 cm^{-1} corresponds to the 2LO band, an overtone of the first order LO phonon [29, 30]. Recent studies [27, 31] have shown that this band has a second weak contribution at 1196 cm^{-1}, that we did not take into account in this study as it does not give additional information. Indeed, this band has the same behaviour as the 1196 cm^{-1} one upon formation of U_4O_9. Bands of very weak intensities are noticeable between 500 and 700 cm^{-1}. These so-called U bands are correlated to the presence of defects in the UO_2 crystallographic structure and to the formation of domains having a

local symmetry lower than the one of perfect UO_2 [32, 33]. The UO_{2+x} spectrum is similar in shape to UO_2 spectrum. A slight blueshift of the T_{2g} band is expected as the result of the UO_2 lattice contraction [34-36]. The insertion of oxygen atoms in the UO_2 fluorite structure entails the presence of defects in the material, which is seen on the Raman spectrum by a slight widening of the T_{2g} peak and an increase of the U defect bands intensity. Different features are observed on the U_4O_9 spectrum. A strong decrease of the T_{2g} intensity and increase of the U bands intensity are observed, while the 2LO band is not visible anymore. We also observe a strong width widening of the T_{2g} band which shifts from ~445 cm^{-1} in UO_2 to ~454 cm^{-1} in U_4O_9.

Thus, strong differences are present between U_4O_9 and UO_2/UO_{2+x} Raman spectra. In particular, the absence/presence of the 2LO band at 1150 cm^{-1} will be used to detect the presence of U_4O_9 in the oxidized pellets. Table 3 summarizes the T_{2g} band position and width measured respectively in the UO_{2+x} and U_4O_9 phases of each oxidized samples.

3.2.1. UO_2 microstructure at low O/U (≤ 2.010)

Figure 2 presents Raman mappings of the *UO2_ox1* sample oxidized consecutively twice. The first oxidation (on the left of the figure) led to a O/U ratio of 2.007 (sample *UO2_ox1_A*) while the second oxidation (on the right of the figure) led to a 2.010 stoichiometry (sample *UO2_ox1_B*). For both O/U ratios, the same region was analyzed by Raman spectroscopy in order to study the evolution of the sample surface morphology. On the optical picture (Figure 2(a)), the region analyzed on sample *UO2_ox1_A* is indicated with a red rectangle while the region analyzed on sample *UO2_ox1_B* corresponds to the whole optical picture. Mappings of the 2LO band intensity are displayed in Figure 2(b) and 2(c), respectively. For both samples, we observe black areas of several micrometric size where the 2LO band intensity is very weak. Raman spectra extracted from one of these regions are presented in Figure 3(a) for both samples, they correspond to U_4O_9 species. However, the 2LO band is visible although its intensity is weak, which is probably due to the fact that the zone probed by the laser also detects some UO_{2+x} phase. In these U_4O_9 area, the T_{2g} band position and width values (Table 3) are intermediate between those of UO_2 and U_4O_9.

Outside of the U_4O_9 zones, the 2LO band intensity mapping is quite homogeneous at the surface of the samples. Raman spectra extracted from this region, on the same grain for the two samples (*UO2_ox1_A* and *UO2_ox1_B*), are presented in Figure 3(b), they are identical. For sake of comparison, a spectrum of stoichiometric UO_2 is also shown on the figure. We do not observe significant changes on the T_{2g} band (same position and width, see Table 3) compared to UO_2. However, the defect bands intensity is noticeably higher compared to the stoichiometric UO_2 spectrum.

On both samples, the U_4O_9 phase forms aggregates inside grains, located heterogeneously. Note that no U_4O_9 aggregates are present in grain boundaries. Comparing the first and second oxidation, U_4O_9 aggregates have similar shapes, sizes and locations on samples. It means that during the second oxidation, U_4O_9 clusters have been formed in the same zones than during the first oxidation. This is noticeable considering the experiment carried out: during the second oxidation process at 1600°C, the U_4O_9 phases formed in sample *UO2_ox1_A* has dissolved and then re-crystallized during the sample cooling. Thus, the U_4O_9 crystallization inside grains is not a random process but a reversible process that occurs in defined locations inside UO_2 grains. In addition, the U_4O_9 aggregate size is comparable for both oxidations, which is probably due to the fact that the final O/M ratio after the two oxidation treatments are close (2.007 and 2.010).

Figure 2(d) and Figure 2(e) display the mapping of the T_{2g} band intensity for both oxidized samples. Outside of U_4O_9 clusters, we observe that this T_{2g} intensity depends on grains. This effect is well-known, and is due to the dependance of the T_{2g} intensity on the different crystalline orientations of UO_2

grains [37, 38]. So, the precipitation of U_4O_9 clusters inside grains do not affect the global crystallography within the grain.

We have performed AFM mapping on sample *UO2_ox1_B*. Particular interest was put on regions containing U_4O_9 phase. Figure S3(a) displays the Raman 2LO band intensity mapping which allows locating U_4O_9 zones on the pellet surface. This mapping was used to choose two areas, indicated by white squares on Figure S3(a), where surface mapping was done by AFM. Figure S3(b-e) shows the 2D and 3D topography images. The color scale, from dark to light brown, indicates the roughness contrast at the surface. U_4O_9 zones are clearly visible as darker zones, which means that they correspond to lower planes (up to ~50 nm) than UO_2 zones. So we evidence that the U_4O_9 formation entails a measurable local contraction of the lattice parameter inside UO_2 grains, even if the lattice parameter of both oxides are only slightly different: 5.44 Å for U_4O_9 [13, 39, 40] and 5.47 Å for UO_2 [13, 41, 42].

As a conclusion, for low hyper-stoichiometric UO_2, we evidence the coexistence of UO_2 and U_4O_9 phases. The latter oxide crystallizes inside UO_2 grains as micrometric clusters entailing a local lattice contraction without altering the overall grains' crystallography.

3.2.2. Effect of quenching on the U_4O_9 formation

Quenching is a rapid cooling process which strongly limits the atomic displacements and the phase transformation. It permits to obtain at room temperature crystallographic phases formed at high temperature. Therefore, quenching, instead of a slow decrease of the temperature, is an effective process to overcome the precipitation of U_4O_9 formed during a heating treatment [13, 20, 43]. Sample *UO2_ox2* was first submitted to an oxidative annealing in order to obtain a O/U = 2.010. Then, it was submitted to a second thermal treatment at a temperature that entails the dissolution of the U_4O_9 phase (900°C), followed by a quenching. No weight evolution of the pellet was measured before and after the quenching, indicating that the O/U ratio did not change during the experiment.

Raman spectroscopy was used to analyze the sample before and after quenching (Figure 4). Before quenching (Figure 4(a)(c)), Raman mapping of the 2LO band intensity (Figure 4(c)) evidences in black the presence of U_4O_9 clusters, as characterized previously. Interestingly, it is possible to see the shape of the U_4O_9 region on the optical picture with a weak contrast of color between U_4O_9 and UO_2 (see white circles). Figure 4(b) and (d) present the optical picture and the corresponding 2LO band intensity mapping performed in the same zone after quenching from 900°C. We observe the disappearance of the U_4O_9 aggregates. Thus, the sample is solely composed of a $UO_{2.01}$ phase.

As observed previously for sample *UO2_ox1*, the Raman mapping exhibits two vibrational signatures, U_4O_9 and UO_{2+x}, before quenching. After quenching, only the UO_{2+x} vibrational signature is present. Figure 5 presents the average spectra of UO_{2+x} zones on the Raman mapping before (mapping without U_4O_9 areas) and after quenching (whole mapping). Their shapes are identical excepting a strong increase of the defect bands intensity after quenching. It can be explained by the dissolution of U_4O_9 aggregates at 900°C, and the incorporation of oxygen atoms in the UO_{2+x} lattice which increases the defects concentration. This phenomenon is also visible by the slight widening of the T_{2g} band from 15.8 to 16.2 cm^{-1} and a slight but significant shift in the T_{2g} band position (cf. Table 3).

3.2.3. Oxidized UO_2 microstructure for O/U = 2.050

Raman mappings of the sample *UO2_ox3* are presented in Figure 6. According to mass gain measurements, this sample has an average hyper-stoichiometry of 2.05 while HERFD-XANES analysis shows that its hyper-stoichiometry in the first micrometer is slightly higher at 2.08. It corresponds to the presence of about 30 % of U_4O_9 in the sample. This latter result is confirmed by the Raman analysis. Indeed, the 2LO band mapping intensity (Figure 6(b)) highlights numerous dark spots distributed over the sample surface, which correspond mainly to U_4O_9 as can be seen on the Raman spectrum extracted from one of the black pixels (Figure S4). In this sample, U_4O_9 does not form big clusters inside grains as shown previously for lower stoichiometric samples, but is present in a rather homogeneous distribution as very small clusters inside grains (cf. Figure 6(b)). Figure S3 also presents a spectrum extracted from a green pixel of the mapping; it is typical of a UO_{2+x} phase and exhibits a shift of the T_{2g} band to 445.1 cm^{-1}. It is interesting to note that these UO_{2+x} zones correspond mainly to grain boundaries, where only few U_4O_9 is detected. Grains are slightly visible on the Raman mapping of the T_{2g} band intensity (Figure 6(c)). So, despite the presence of about 30 % of U_4O_9, the grain crystalline orientation is somehow maintained and the fluorite structure remains present.

3.2.4. Oxidized UO_2 microstructure for O/U = 2.10

Sample *UO2_ox4* was prepared with a final hyper-stoichiometry of 2.10, following the protocol explained in the experimental section (2.2). HERFD-XANES analysis shows that it contains about 65% of U_4O_9 on the first micrometer that results in a hyper-stoichiometry of 2.16. Its Raman mappings are presented in Figure 7. The 2LO band intensity mapping displays dark areas distributed as a zebra pattern on the sample surface. We do not see any difference between grain and grain boundaries. As shown in Figure 8, these dark areas correspond to pure U_4O_9. Elsewhere on the pellet, Raman spectra show the presence of UO_{2+x}. A spectrum, extracted on a green pixel of the mapping, is shown in Figure 8. A noticeable shift of the T_{2g} band position in the UO_{2+x} area is measured at 445.7 cm^{-1}, larger than the one measured at x=2.05. So, as the global hyper-stoichiometry increases, the proportion of U_4O_9 as well as the hyper-stoichiometry of the UO_{2+x} phase increase. The T_{2g} band intensity mapping is displayed in Figure 8(c). Despite the large U_4O_9 concentration, it is still possible to distinguish the contrast between grains in the UO_{2+x} phase. So as observed at lower hyper-stoichiometries, the UO_2 lattice is maintained despite the growth of U_4O_9 phase.

3.2.5. UO_{2+x} phase composition as a function of the sample hyper-stoichiometry

Table 3 summarizes the T_{2g} band position measured in UO_{2+x} phase of oxidized samples, and we observe that this position shifts with the global hyper-stoichiometry of samples. Thanks to these measurements, it is possible to evaluate the O/M ratio specifically in UO_{2+x} phases of our samples. Indeed, the increase of hyper-stoichiometry entails a contraction of the fluorite lattice parameter [13]. This effect has a direct impact on the T_{2g} band position which is expected to shift to higher frequencies according to the following relation [44]:

$$\Delta T_{2g} = -3\gamma\omega\frac{\Delta a}{a_0} \qquad (1)$$

where γ is the Gruneisen parameter (2.17 for UO_2), ω is the T_{2g} position for stoichiometric UO_2, Δa is the variation of the lattice parameter compared to the UO_2 one (a_0).

Therefore, knowing the T_{2g} band position shift from pristine UO_2 (ΔT_{2g}), it is possible to determine the corresponding variation of the lattice parameter (Δa) [45], and thus, to evaluate the O/M ratio in

the UO_{2+x} phase. Indeed, the variation of the UO_{2+x} lattice parameter as a function of x has been widely reported in the literature [34]. Results are given in Table 4 where they are compared with the O/U ratio calculated for the whole pellet from mass gain after oxidative treatments. For low oxidized samples, (*UO2_ox1* and *UO2_ox2_BQ*), the T_{2g} band shift measured in the UO_{2+x} phase inside grains is within uncertainties and as a matter of fact, the corresponding O/U is close to 2. It means that in these samples, most of additional oxygen atoms have formed U_4O_9 phase while the "UO_{2+x} phase" is stoichiometric or nearly. In sample *UO2_ox2_AQ* formed by a sole UO_{2+x} phase, the O/U value obtained by Raman measurement is in line with the one obtained by mass gain measurement, i.e. ~2.01. For samples *UO2_ox3* and *UO2_ox4*, O/U ratios of the UO_{2+x} phase increase with the global hyper-stoichiometry of the samples (respectively 2.010 and 2.023) and correspond roughly to 20% of the global O/U ratio.

4. Discussion

We have carried out a study consisting in oxidizing UO_2 pellets, initially stoichiometric, to hyper-stoichiometries up to 2.1. As expected from the U-O phase diagram, we have characterized two crystallographic phases, UO_{2+x} and U_4O_9, by coupling HERFD-XANES and Raman spectroscopy measurements at room temperature. A significant discrepancy is observed between the calculated O/U ratios from XANES measurements and the one obtained from the mass gain of samples for the most oxidized sample at 2.1. Indeed, the hyper-stoichiometry is higher at the extreme surface of the sample (XANES probes the first micrometer) than expected. Contrary to other samples, its thermal treatment was performed at 850°C, not at 1600°C. At 1600°C, the oxygen diffusion coefficient (D) in stoichiometric polycrystalline UO_2 pellets is in the order of 10^{-6} cm²/s [46]. So, a constant repartition of oxygen over the whole pellet depth is obtained after a 4-hour annealing and the hyper-stoichiometry can be considered as constant inside the sample. It may not be the case at 850°C for a 3.5 hour annealing. The oxygen diffusion coefficient is significantly lower at this temperature, in the order of 10^{-11}-10^{-12} cm²/s according to authors [46-48]. It corresponds to a diffusion of oxygen over the first ~20 µm in sample *UO2_ox4*. However, it is known that the increase of UO_2 stoichiometry entails a significant increase of O diffusion. Large discrepancies exist in the literature concerning oxygen diffusion coefficients in UO_{2+x} probably because of the different experimental protocols used to make D measurements [49-52]. According to those data, the oxygen diffusion coefficient may range between 10^{-8} and 10^{-13} cm²/s at 850°C. Therefore, it is difficult to evaluate precisely the diffusion depth of oxygen in sample *UO2_ox4*. It is expected to be above 20 µm but may not be large enough to assure a constant repartition of oxygen over the whole depth. This question will be addressed in a further work by the characterization of pellet cross-sections.

Some authors noticed a preferential oxidation as a function of the grain orientation, based on works by Allen et al. on UO_2 single-crystals [53, 54]. We do not observe this phenomenon, the amount of U_4O_9 being homogeneous at the pellet surface whatever the O/U. However, the experimental conditions used by Allen (300°C, 1 torr of O_2) are significantly different from ours and led to the formation of upper oxides (U_3O_7 and U_3O_8) not observed in our work. It highlights also the effect of the oxidative conditions on the nature of the oxides formed. In our study, oxidative annealing treatments have been performed at 1600°C or 850°C, i.e. temperatures where the sole existing phase is UO_{2+x}. The crystallographic phases we further characterized at room temperature are the one "allowed" to form during the sample cooling, i.e. UO_{2+x} and U_4O_9 according to the U-O phase diagram. When oxidation treatments are performed at lower temperature and under stronger oxidative conditions like air, a prompt conversion of U_4O_9 into U_3O_7 and eventually U_3O_8 is observed [55-57].

Thanks to the analysis of Raman mapping, we could evaluate the composition of the UO_{2+x} phases as a function of the global O/U ratio of samples, while XANES could help evaluate the proportion of U_4O_9 inside samples. At low O/U (~0.01), the UO_{2+x} phase can be considered as stoichiometric, which

means that samples are composed of UO_2 and ~10% of U_4O_9. For O/U ≥ 2.05, samples are composed of U_4O_9 and of a UO_{2+x} phase whose hyper-stoichiometry increases with the global O/U ratio. For O/U = 2.05, samples are composed of ~70% of $UO_{2.01}$ and ~30 % of U_4O_9 while at O/U = 2.1, it is composed of ~65% U_4O_9 and 35% $UO_{2.02}$. We thus observe that UO_{2+x} phases display quite low O/M ratios, even for high global hyper-stoichiometries.

We could evidence the U_4O_9 growth mechanism inside grains. At low hyper-stoichiometry (2.01), U_4O_9 is present as micrometric clusters inside stoichiometric UO_2 grains. These clusters are formed during the slow cooling of our sample from a homogeneous UO_{2+x} phase. Such clusters were evidenced by Allen et al. [58] but for highly oxidized UO_2 pellet, at O/U = 2.24. As the hyper-stoichiometry increases to O/U = 2.1, these clusters coalesce to form a U_4O_9 network at the surface of the material. This kind of microstructure can be compared to those reported by previous works, showing that the precipitation of U_4O_9 in UO_{2+x} leads to a Widmanstätten needle structure or the formation of platelets [59] [17, 19, 20]. The formation of U_4O_9 entails a local lattice contraction inside grains, evidenced by AFM, but without affecting the surrounding UO_2 matrix. Even for high hyper-stoichiometry (x>2.1) where U_4O_9 is the main crystallographic phase, the UO_2 lattice is preserved and as a result, we always observe a joint presence of two crystallographic phases. In this respect, this is comparable with observations made by Allen [58] on UO_2 pellets and Leinders [60] on UO_2 nanopowders. We also show by oxidizing twice a UO_2 sample at high temperature (1600°C) that U_4O_9 clustering inside UO_2 grains is not a random process and that it occurs in defined zones inside grains. One may link this fact with the presence of defects in grains that may constitute nucleation sites. The precipitation of U_4O_9 in UO_{2+x} occurs by agglomeration of oxygen atoms that produces defects. For this reason, some authors consider that the interface between UO_{2+x} and U_4O_9 is equivalent to dislocations [61]. One may envision that after re-dissolution of U_4O_9, dislocations remain and, during the second oxidation annealing, favor the recrystallisation of U_4O_9 in the same zone of grains. We have also observed that the formation of U_4O_9 occurs only inside grains, not in grain boundaries. The latter contain a high concentration of defects like dislocations that entails a lower crystallinity, and probably, tensile strains, that may entail the clustering of U_4O_9.

5. Conclusion

We have studied the UO_{2+x}/U_4O_9 phase equilibrium in UO_2 in the hyper-stoichiometry range $0.01<x<0.1$, after thermal oxidation treatments performed under dry conditions at 850°C or 1600°C. By coupling HERFD-XANES at the uranium M_4-edge and micro-Raman spectroscopy mapping, we could determine the proportion between each phase and their composition.

At low O/U, U_4O_9 is present as small clusters inside UO_2 grains. Their formation, occurring during the slow cooling of our samples, does not occur in random area of grains. Indeed, we show, by repeating twice the annealing/cooling process, that the U_4O_9 cluster size and location are identical. The presence of U_4O_9 entails a local contraction of the lattice, measurable by AFM, which does not affect the global structure of grains even at high U_4O_9 concentration.

As the O/U increases, the proportion of U_4O_9 and the UO_{2+x} phase hyper-stoichiometry increase, leading to the formation of a network of U_4O_9 crystallized inside UO_{2+x} grains. However, even for highly oxidized samples, we evidence that the UO_{2+x} phases exhibit only a slight O/M, meaning that during the slow cooling process, most of the additional oxygen atoms are incorporated as U_4O_9 in the samples.

Data availability statement

Data will be made available on request.

Funding

The authors acknowledge the support of the French Agence Nationale de la Recherche (ANR), under grant ANR-21-CE05-0035 (project BENEFICIA).

Acknowledgments

We acknowledge Dr S. Forel (LMI, UCBL, France) for her assistance using AFM, Dr M. Pijolat, V. Péres and L. Vieille (Mines St Etienne, France) for the TGA experiments. The authors would also like to thank R. Fillol (IP2I) for his helpful technical contribution.

We acknowledge SOLEIL for provision of synchrotron radiation facilities and we would like to thank Dr M. Hunault and Dr P-L. Solari for assistance in using beamline MARS.

Conflict of Interest

The authors declare that the research was conducted in the absence of any commercial or financial relationships that could be construed as a potential conflict of interest.

Author Contributions

C. Gaillard: Conceptualization, formal analysis, funding acquisition, investigation, project administration, supervision, writing – original draft.
H. Lotz: formal analysis, investigation, writing-original draft.
L. Sarrasin: investigation, formal analysis.
Y. Pipon: funding acquisition, writing-review & editing.
R. Ducher: funding acquisition, writing-review & editing.
N. Moncoffre: funding acquisition, writing-review & editing.

References

[1] D. Horlait, J. Domange, M.-L. Amany, M. Gérardin, M.-F. Barthe, G. Carlot, E. Gilabert, Experimental investigation of Kr diffusion in UO_{2+x} : Slight deviations from stoichiometry, significant effects on diffusion kinetics and mechanisms, J. Nucl. Mater., 574 (2023) 154191.

[2] T. Kudo, M. Kida, T. Nakamura, F. Nagase, T. Fuketa, Effects of fuel oxidation and dissolution on volatile fission product release under severe accident conditions, J. Nucl. Sci. Technol., 44 (2007) 1428.

[3] C. Le Gall, F. Audubert, J. Lechelle, Y. Pontillon, J.-L. Hazemann, Contribution to the study of fission products release from nuclear fuels in severe accident conditions: effect of the pO_2 on Cs, Mo and Ba speciation, EPJ Nuclear Sci. Technol., 6 (2020) 2.

[4] P. Taylor, Thermodynamic and kinetic aspects of UO_2 fuel oxidation in air at 400-2000 K, J. Nucl. Mater., 344 (2005) 206.

[5] R.J. Mc Eachern, P. Taylor, A review of the oxidation of uranium dioxide at temperatures below 400°C, J. Nucl. Mater., 254 (1998) 87.

[6] G. Rousseau, L. Desgranges, F. Charlot, N. Millot, J.C. Nièpce, M. Pijolat, F. Valdivieso, G. Baldinozzi, J.F. Bérar, A detailed study of UO_2 to U_3O_8 oxidation phases and the associated rate-limiting steps, J. Nucl. Mater., 355 (2006) 10.

[7] L. Desgranges, G. Baldinozzi, D. Siméone, H.E. Fischer, Refinement of the α-U_4O_9 crystalline structure: new insight into the U_4O_9 -> U_3O_8 transformation, Inorg. Chem., 50 (2011) 6146.

[8] F. Garrido, L. Nowicki, L. Thomé, Channeling investigation of the crystalline structure of U_4O_{9-y}, Phys. Rev. B, 74 (2006) 184114.

[9] A. Soulié, G. Baldinozzi, F. Garrido, J.-P. Crocombette, Clusters of Oxygen Interstitials in UO_{2+x} and α-U_4O_9: Structure and Arrangements, Inorg. Chem., 58 (2019) 12678.

[10] R.J. Mc Eachern, A review of kinetic data on the rate of U_3O_7 formation on UO_2, J. Nucl. Mater., 245 (1997) 238.

[11] M.J. Bannister, W.J. Buykx, A dilatometric study of the solubility of U_4O_9 in UO_2, J. Nucl. Mater., 55 (1974) 345.

[12] P.E. Blackburn, Oxygen dissociation pressures over uranium oxides, J. Phys. Chem., 62 (1958) 897.

[13] F. Gronvold, High-temperature X-ray study of uranium oxides in the UO_2 - U_3O_8 region, J. Inorg. Nucl. Chem., 1 (1955) 357.

[14] C. Guéneau, M. Baichi, D. Labroche, C. Chatillon, B. Sundman, Thermodynamic assessment of the uranium-oxygen system, J. Nucl. Mater., 304 (2002) 161.

[15] J.D. Higgs, W.T. Thompson, B.J. Lewis, S.C. Vogel, Kinetics of precipitation of U_4O_9 from hyperstoichiomectric UO_{2+x}, J. Nucl. Mater., 366 (2007) 297.

[16] T. Ishii, K. Naito, K. Oshima, X-ray study on a phase transition and a phase diagram on the U_4O_9 phase, Solid State Commun., 8 (1970) 677.

[17] W.V. Lierde, J. Pelsmaekers, A. Lecocq-Robert, On the phase limits of U_4O_9, J. Nucl. Mater., 37 (1970) 276.

[18] T. Matsui, K. Naito, Phase relation and defect structures of nonstoichiometric $U_4O_{9+/-y}$ and UO_{2+x} at high temperature, J. Nucl. Mater., 56 (1975) 327.

[19] S. Whillock, J.H. Pearce, A method of determining the distribution of U_4O_9 in oxidised UO_2, J. Nucl. Mater., 175 (1990) 121.

[20] B.E. Schaner, Metallographic determination of the UO_2-U_4O_9 phase diagram, J. Nucl. Mater., 2 (1960) 110.

[21] T.B. Lindemer, T.M. Besmann, Chemical thermodynamic representation of $UO_{2+/-x}$, J. Nucl. Mater., 130 (1985) 473.

[22] B. Sitaud, P.L. Solari, S. Schlutig, I. Llorens, H. Hermange, Characterization of radioactive materials using the MARS beamline at the synchrotron SOLEIL, J. Nucl. Mater., 425 (2012) 238.

[23] B. Ravel, M. Newville, ATHENA, ARTEMIS, HEPHAESTUS: data analysis for X-ray absorption spectroscopy using IFEFFIT, J. Synchrotron Rad., 12 (2005) 537-541.

[24] T.R. Griffiths, H.V. St.A. Hubbard, Absorption spectrum of single-crystal UO_2: Identification of and effect of temperature on the peak positions of essentially all optical transitions in the visible to near infrared regions using derivative spectroscopy, J. Nucl. Mater., 185 (1991) 243.

[25] K.O. Kvashnina, S.M. Butorin, High-energy resolution X-ray spectroscopy at actinide $M_{4,5}$ and ligand K edges: what we know, what we want to know, and what we can know, Chem. Comm., 58 (2022) 327.

[26] G. Leinders, R. Bes, K.O. Kvashnina, M. Verwerft, Local structure in U(IV) and U(V) environments: the case of U_3O_7, Inorg Chem, 59 (2020) 4576.

[27] C. Gaillard, L. Sarrasin, C. Panetier, Y. Pipon, R. Ducher, N. Moncoffre, Isotopic effect of oxygen on the Raman mapping of a polycrystalline uranium dioxide UO_2, J. Raman Spectrosc., (2024) 1.

[28] V.G. Keramidas, W.B. White, Raman spectra of oxides with the fluorite structure, J. Chem. Phys., 59 (1973) 1561.

[29] T. Livneh, E. Sterer, Effect of pressure on the resonant multiphonon Raman scattering in UO_2, Phys. Rev. B, 73 (2006) 085118.

[30] J.M. Elorrieta, L.J. Bonales, V.G. Baonza, J. Cobos, Temperature dependence of the Raman spectrum of UO_2, J. Nucl. Mater., 503 (2018) 191.

[31] T. Livneh, Resonant Raman scattering in UO_2 revisited, Phys. Rev. B, 105 (2022) 045115.

[32] G. Guimbretière, L. Desgranges, A. Canizarès, G. Carlot, R. Caraballo, C. Jégou, P. Simon, Determination of in-depth damaged profile by Raman line scan in a pre-cut He^{2+} irradiated UO_2, Appl. Phys. Lett., 100 (2012) 251914.

[33] P. Simon, A. Canizarès, N. Raimboux, L. Desgranges, How can Raman spectroscopy be used to study nuclear fuel?, MRS Bulletin, 48 (2023) 1.

[34] J. Spino, P. Peerani, Oxygen stoichiometry shift of irradiated LWR-fuels at high burn-ups: Review of data and alternative interpretation of recently published results, J. Nucl. Mater., 375 (2008) 8.

[35] G.C. Allen, P.A. Tempest, J.W. Tyler, Coordination model for the defect structure of hyperstoichiometric UO_{2+x} and U_4O_9, Nature, 295 (1982) 48.

[36] H. He, D. Shoesmith, Raman spectroscopic studies of defect structures and phase transition in hyper-stoichiometric UO_{2+x}, Phys. Chem. Chem. Phys., 12 (2010) 8108.

[37] P.K. Morgan, T.A. Prusnick, M.A. Velez, K. Rickert, D.B. Turner, J.M. Mann, Identifying crystallographic faces of the fluorites urania and thoria with rotational polarized Raman spectroscopy, J. Raman Spectrosc., 52 (2021) 1902.

[38] O.A. Maslova, X. Iltis, L. Desgranges, M.R. Ammar, C. Genevois, E.d. Bilbao, A. Canizarès, S.A. Barannikova, I.N. Leontyev, P. Simon, Characterization of an UO_2 ceramic via Raman imaging and electron backscattering diffraction, Material characterization, 147 (2019) 280.

[39] G.C. Allen, N.R. Holmes, A mechanism for the UO_2 to α-U_3O_8 phase transformation, J. Nucl. Mater., 223 (1995) 231.

[40] R.I. Cooper, B.T.M. Willis, Refinement of the structure of β-U_4O_9, Acta Crystallogr.,Sect.A, A60 (2004) 322.

[41] L. Desgranges, G. Baldinozzi, G. Rousseau, J.C. Nièpce, G. Calvarin, Neutron diffraction study of the in situ oxidation of UO_2, Inorg Chem, 48 (2009) 7585.

[42] G. Leinders, T. Cardinaels, K. Binnemans, M. Verwerft, Accurate lattice parameter measurements of stoichiometry uranium, J. Nucl. Mater., 459 (2015) 135.

[43] T. Yao, S.M. Scott, G. Xin, B. Gong, J. Lian, Dense nanocrystalline UO_{2+x} fuel pellets synthetized by high pressure spark plasma sintering, J. Am. Ceram. Soc., 101 (2018) 1105.

[44] J.R. McBride, K.C. Hass, B.D. Poindexter, W.H. Weber, Raman and x-ray studies of $Ce_{1-x}RE_xO_{2-y}$, where RE=La, Pr, Nd, Eu, Gd, and Tb, J. Appl. Phys., 76 (1994) 2435.

[45] L. Medyk, D. Manara, J.Y. Colle, D. Bouexière, J.-F. Vigier, L. Marchetti, P. Simon, P. Martin, Determination of the plutonium content and O/M ratio of (U,Pu)O 2-x using Raman spectroscopy, J. Nucl. Mater., 541 (2020).

[46] A.C.S. Sabioni, W.B. Ferraz, F. Millot, Effect of grain boundaries on uranium and oxygen diffusion in polycrystalline UO_2, J. Nucl. Mater., 278 (2000) 364.

[47] B. Dorado, P. Garcia, G. Carlot, M. Fraczkiewicz, B. Pasquet, M. Freyss, C. Valot, G. Baldinozzi, D. Siméone, M. Bertolus, First-principles calculation and experimental study of oxygen diffusion in uranium dioxide, Phys. Rev. B, 83 (2011) 035126.

[48] C. Berthinier, C. Rado, C. Chatillon, F. Hodaj, Thermodynamic assessment of oxygen diffusion in non-stoichiometric $UO_{2+/-x}$ from experimental data and Frenkel pair modeling, J. Nucl. Mater., 433 (2013) 265.

[49] J.T. Bittel, I.H. Sjodahi, J.F. White, Steam oxidation kinetics and oxygen diffusion in UO2 at high temperatures, J. Am. Ceram. Soc., 52 (1969) 446.

[50] A.S. Bayoglu, R. Loreznzelli, Oxygen diffusion in fcc fluorite type nonstoichiometric nuclear oxides $MO_{2+/-x}$, Sol. State Ion., 12 (1984).

[51] K.W. Lay, Oxygen chemical diffusion coefficient of uranium dioxide, J. Am. Ceram. Soc., 53 (1970) 369.

[52] P. Ruello, G. Chirlesan, G. Petot-Ervas, C. Petot, L. Desgranges, Chemical diffusion in uranium dioxide - influence of defect interactions, J. Nucl. Mater., 325 (2004) 202.

[53] G.C. Allen, P.A. Tempest, J.W. Tyler, Characterisation of crystalline UO_2 oxidised in 1 torr of oxygen at 25, 225 and 300°C ; Part 1. X-Ray Photoelectron Spectroscopy, J. Chem. Soc., Faraday Trans., 84 (1988) 4049.

[54] G.C. Allen, P.A. Tempest, J.W. Tyler, Characterization of crystalline UO_2 oxidized in 1 Torr of oxygen at 25, 225 and 300°C ; Part 2. X-ray diffraction and Scanning electron Microscopy, J. Chem. Soc., Faraday Trans., 84 (1988) 4061.

[55] E. De Bona, K. Popa, O. Walter, M. Cologna, C. Hennig, A.C. Scheinost, D. Prieur, Oxidation of Micro- and Nanograined UO_2 Pellets by In Situ Synchrotron X-ray Diffraction, Inorg. Chem., 61 (2022) 1843.

[56] A. Milena-Perez, N. Rodriguez-Villagra, S. Fernandez-Carretero, A. Nunez, Thermal air oxidation of UO_2: Joint effect of precursor's nature and particle

size distribution, Prog. Nucl. Ener., 159 (2023) 104629.

[57] S.R. Teixeira, K. Imakuma, High temperature X-ray diffraction study of the U_4O_9 formation on UO_2 sintered plates, J. Nucl. Mater., 178 (1991) 33.

[58] G.C. Allen, J.T. Buswell, P.A. Tempest, Ordering phenomena in U_4O_{9-y} crystals studied by Transmission electron Microscopy, J. Chem. Soc., Dalton Trans., (1983) 589.

[59] R.H. Tuxworth, W. Evans, Habit planes for U_4O_9 precipitation in uranium dioxide, J. Nucl. Mater., 3 (1959) 302.

[60] G. Leinders, J. Pakarinen, T. Delville, K. Binnemans, M. Verwerft, Low-temperature oxidation of fine UO_2 powders: a process of nanosized domain development, Inorg Chem, 55 (2016) 3915.

[61] H. Chevrel, Frlttage à basse temperature du dioxyde d'uranium, en conditions de sur-stoechiometrie temporaire, Rapport CEA R-5569, (1992).

Table 1: Summary of the sample oxidative treatments

Sample ID	O/U ratio	Sample oxidative treatment
UO_2	2.000	-
UO2_ox1_A	2.007	4h – 1600°C – Ar/O_2 5 ppm
UO2_ox1_B	2.010	4h + 4h – 1600°C – Ar/O_2 5 ppm
UO2_ox2_BQ	2.010	4h + 4h – 1600°C – Ar/O_2 5 ppm
UO2_ox2_AQ	2.010	4h + 4h – 1600°C – Ar/O_2 5 ppm, quenching at 900°C
UO2_ox3	2.050	15h – 1600°C – Ar/O_2 5 ppm
UO2_ox4	2.100	2h – 850°C – Ar/O_2 100 ppm during plateau temperature

Table 2: Proportion between U(IV) and U(V) and stoichiometries in UO_2 oxidized samples, obtained by linear fitting of HERFD-XANES spectra using two reference compounds UO_2 and U_4O_9. The average O/U ratio was obtained by mass gain measurements after the oxidation treatments.

Sample ID	Average O/U*	% UO_2	% U_4O_9	% U(IV)	% U(V)	XANES O/U ratio (± 0.01) on the first µm
UO_2	2.000	100	0	100	0	2.00
UO2_ox1_B	2.010	90	10	95	5	2.02
UO2_ox3	2.050	70	30	85	15	2.08
UO2_ox4	2.100	35	65	67	33	2.16

*obtained by mass gain measurements

Table 3: Summary of the T_{2g} band position and width in UO_2/UO_{2+x} and U_4O_9 phases (BQ = Before Quenching, AQ = After Quenching, cf. part 2.2).

	UO_2 - UO_{2+x} phase		U_4O_9 phase	
	Position (cm^{-1})	Width (cm^{-1})	Position (cm^{-1})	Width (cm^{-1})
UO_2	444.6	15.7	-	-
U_4O_9	-	-	455	45
UO2_ox1_A	444.7	15.7	448	27
UO2_ox1_B	444.7	15.7	449	30
UO2_ox2 BQ	444.8	15.8	452	40
UO2_ox2 AQ	444.9	16.2	-	-
UO2_ox3	445.1	15.8	450	30
UO2_ox4	445.7	16.8	457	45

Table 4: Calculation of lattice parameters A and O/U ratio in the UO_{2+x} phase of analyzed samples, from the T_{2g} band shift ΔT_{2g}. For sake of comparison, O/U ratio obtained by mass gain are given.

	UO_{2+x} phase			Average in the sample
Sample ID	ΔT_{2g} (cm^{-1})	Calculated A (Å)	Calculated O/U	O/U from mass gain
UO2	0	5.4703	2.000	2.00
UO2_ox1_A	0.1	5.4701	2.002	2.007
UO2_ox1_B	0.1	5.4701	2.002	2.01
UO2_ox2 BQ	0.2	5.4699	2.004	2.01
UO2_ox2 AQ	0.3	5.4697	2.007	2.01
UO2_ox3	0.5	5.4693	2.010	2.05
UO2_ox4	1.1	5.4682	2.023	2.10

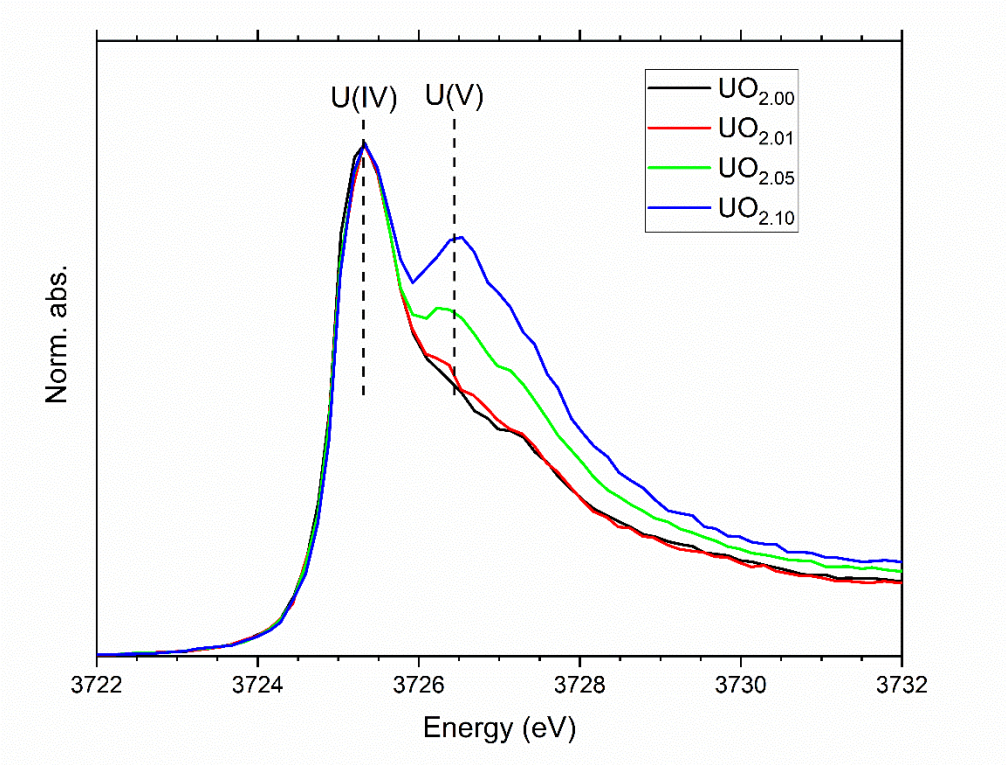

Figure 1: HERFD-XANES spectra at the U M_4-edge of stoichiometric UO_2 and oxidized UO_2 samples at different O/U (see Table 1 for sample details).

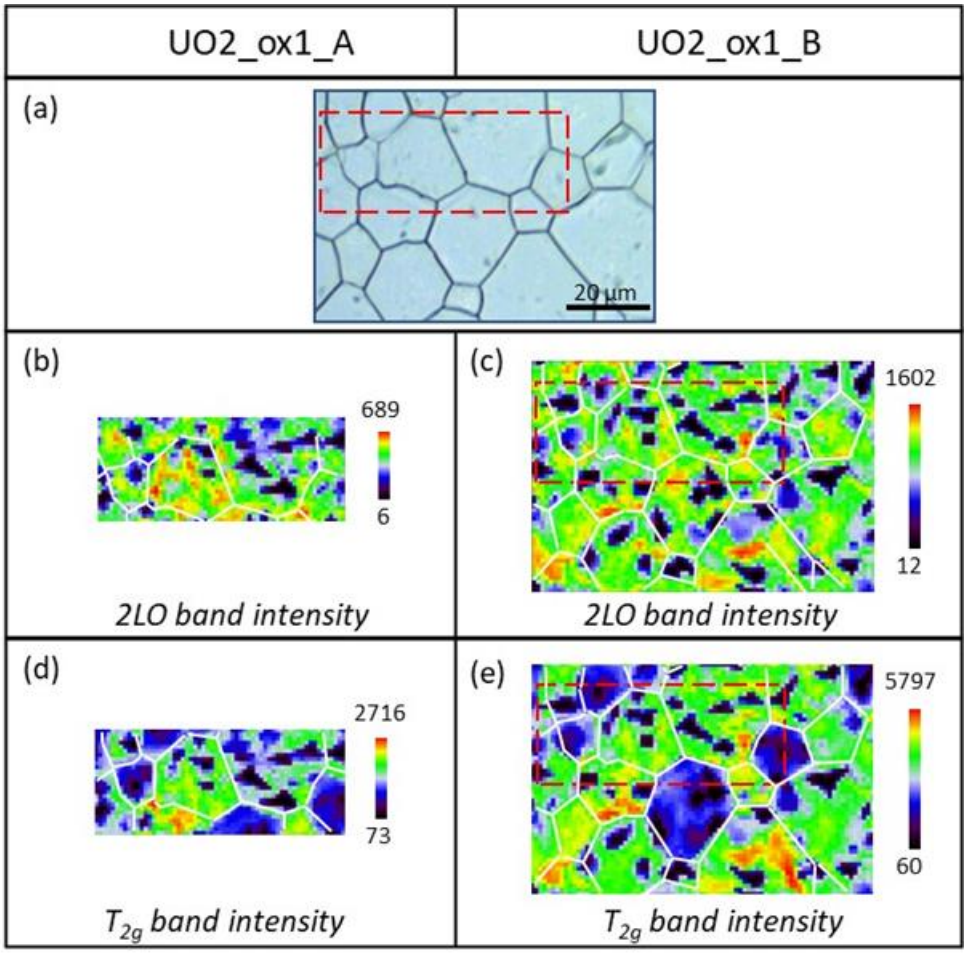

Figure 2: Raman mappings of the 2LO and T_{2g} band intensity at the surface of sample *UO2_ox1* after 2 oxidations (samples *UO2_ox1_A* on the left and *UO2_ox1_B* on the right). (a) Optical picture of the analysed region; (b) and (c) Raman mapping of the 2LO band intensity; (d) and (e) Raman mapping of the T_{2g} band intensity. The colour scale corresponds to the intensity scale, from the lowest (black) to the highest (red) value. For sake of clarity, grain boundaries visible on the optical picture are represented by white lines on mappings.

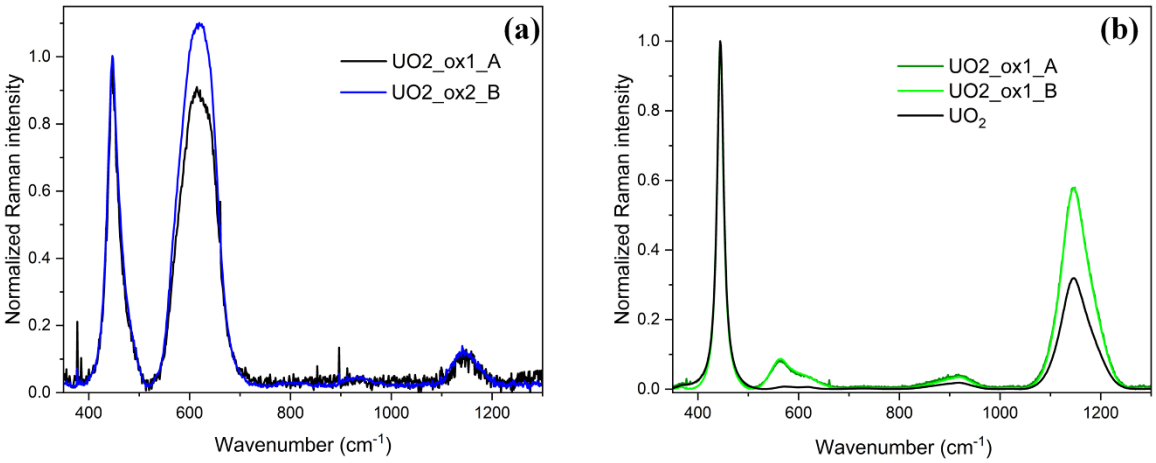

Figure 3: Raman spectra extracted from *UO2_ox1_A and UO2_ox1_B sample mappings (cf. Figure 2).* (a) Individual Raman spectra extracted in U_4O_9 area (back pixels on the mapping); (b) Individual Raman spectra extracted in UO_{2+x} area (green pixels on the mapping). Spectra were normalized on the T_{2g} band intensity for sake of comparison.

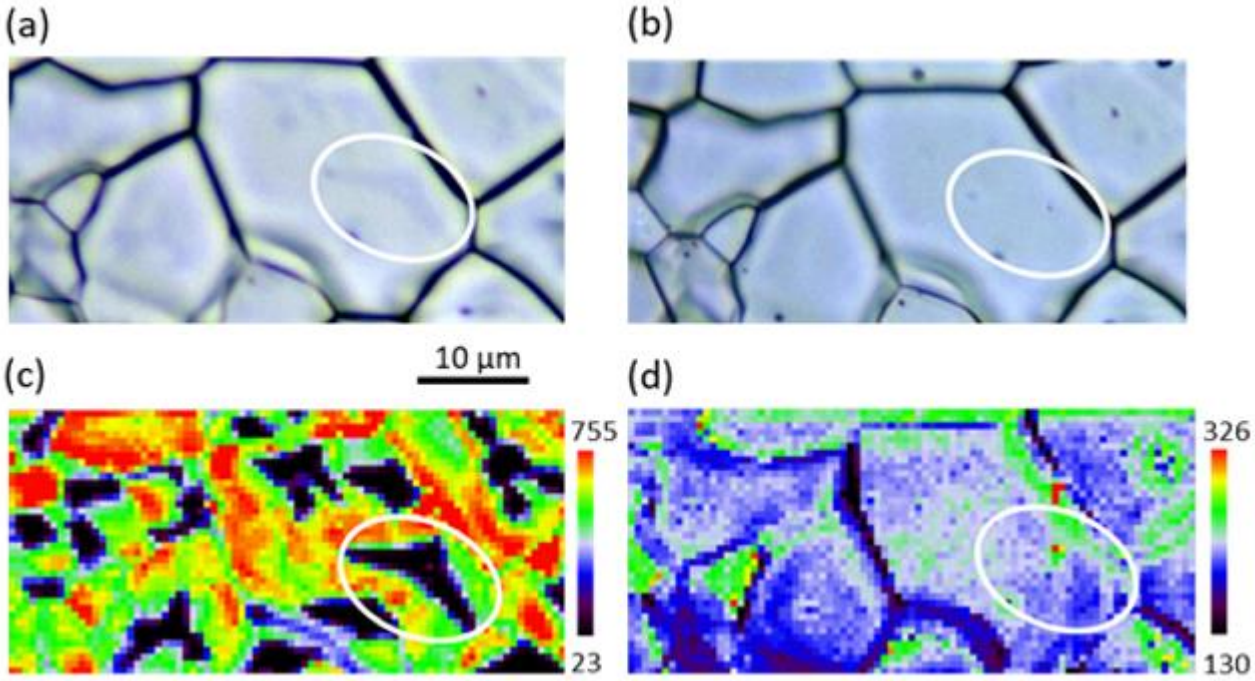

Figure 4: Effect of quenching on the 2LO band intensity Raman mapping of sample *UO2_ox2*. (a) Optical picture of the analyzed zone before and (b) after quenching; (c) and (d) Raman mapping of the 2LO intensity before (c) and after quenching (d).

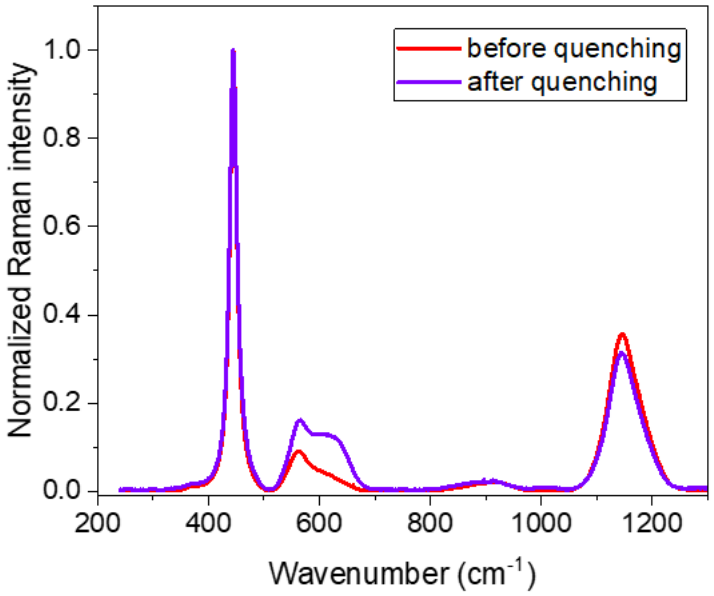

Figure 5: Effect of quenching on the Raman spectra of sample *UO2_ox2*. Average spectra of UO_{2+x} zones on the Raman mapping before quenching (red); average spectrum of the mapping after quenching (blue). For sake of comparison, spectra are normalized to the T_{2g} band intensity.

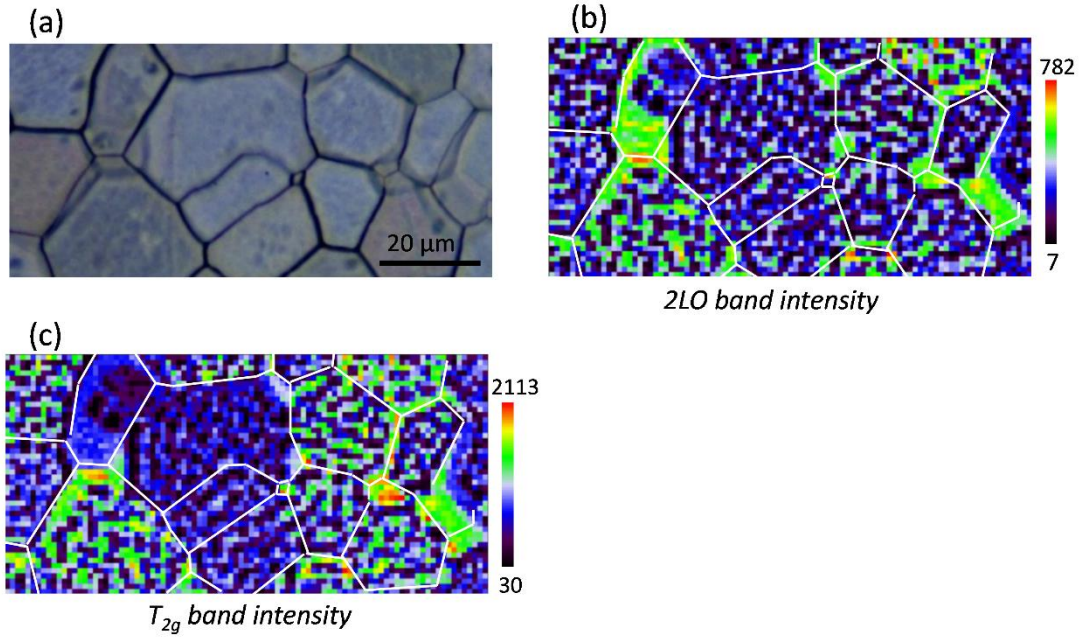

Figure 6: Raman mapping of sample *UO2_ox3*. (a) optical picture of the analyzed zone; (b) 2LO band intensity mapping; (c) T_{2g} band intensity mapping.

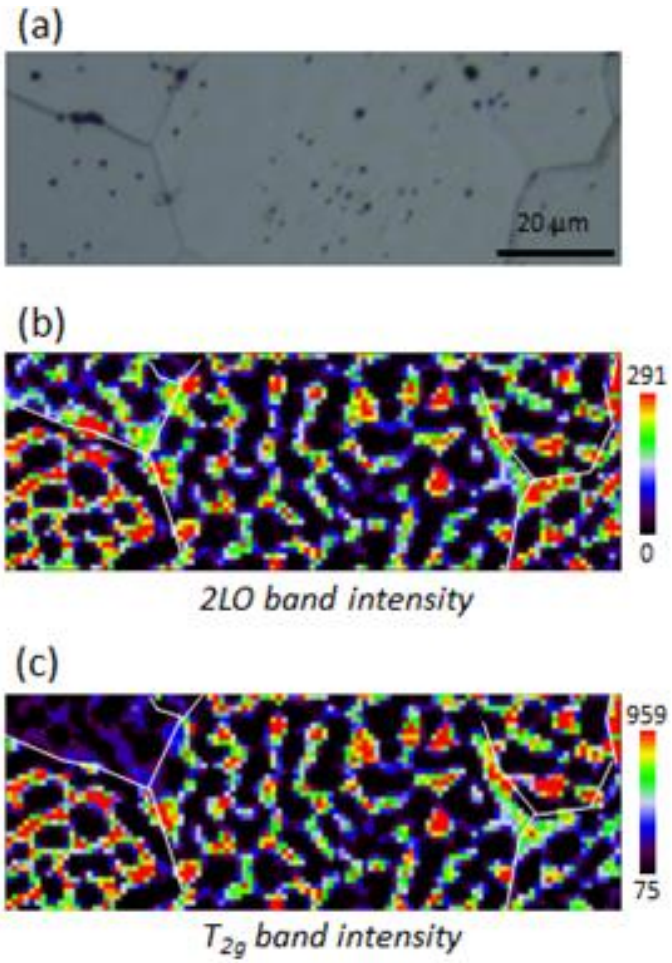

Figure 7: Raman mappings of sample *UO2_ox4*. (a) optical picture of the analyzed zone; (b) 2LO band intensity mapping; (c) T_{2g} band intensity mapping.

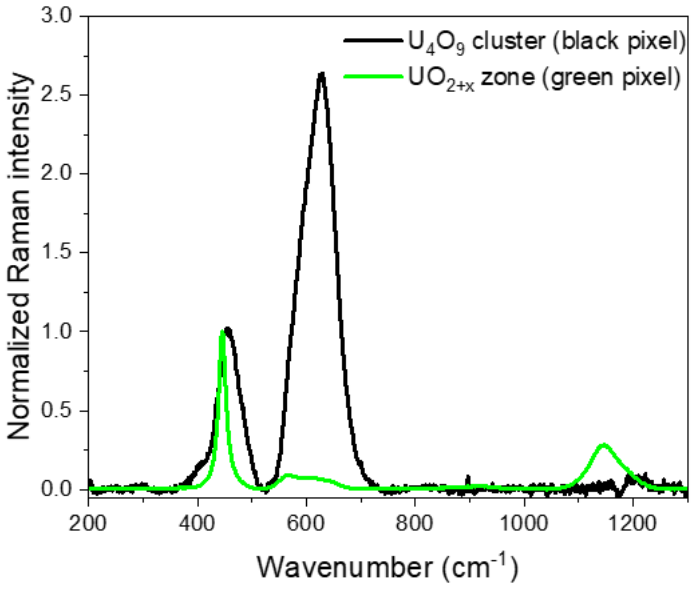

Figure 8: Raman spectra extracted on the mapping of sample *UO2_ox4*, in U_4O_9 clusters (black pixel on the mapping) and in UO_{2+x} zone (green pixel on the mapping). Spectra are normalized to the T_{2g} band intensity.